# Nonlinear electromagnetic formulation for particle-in-cell simulation of lower hybrid waves in toroidal geometry

J. Bao,[1,2] Z. Lin,[2,a)] A. Kuley,[2] and Z. X. Wang[2]
[1]*Fusion Simulation Center, Peking University, Beijing 100871, China*
[2]*Department of Physics and Astronomy, University of California, Irvine, California 92697, USA*

(Received 10 July 2015; accepted 16 May 2016; published online 3 June 2016)

An electromagnetic particle simulation model has been formulated and verified for nonlinear processes of lower hybrid (LH) waves in fusion plasmas. Electron dynamics are described by the drift kinetic equation using either kinetic momentum or canonical momentum. Ion dynamics are treated as the fluid system or by the Vlasov equation. Compressible magnetic perturbation is retained to simulate both the fast and slow LH waves. Numerical properties are greatly improved by using the electron continuity equation to enforce the consistency between electrostatic potential and vector potential, and by using the importance sampling scheme. The simulation model has been implemented in the gyrokinetic toroidal code (GTC), and verified for the dispersion relation and nonlinear particle trapping of the electromagnetic LH waves. *Published by AIP Publishing*. [http://dx.doi.org/10.1063/1.4952773]

## I. INTRODUCTION

The lower hybrid current drive (LHCD) has been successfully predicted[1] and subsequently demonstrated in many fusion experiments.[2] In fact, the lower hybrid (LH) wave is one of the most efficient tools for steady-state operation of a tokamak,[3] as well as to control the current profile and to suppress magneto-hydrodynamic instabilities.[4] Thus, reliable prediction of current profile driven by the LH wave is important for fusion experiments. Many linear and quasi-linear simulation models have been developed to study the LH wave propagation and absorption in tokamaks, such as Wentzel–Kramers–Brillouin (WKB) and full-wave approaches.[5–8] The WKB approach solves Maxwell's equation in the short wavelength limit and gives the asymptotic solution for wave propagation, while the full wave approach solves Maxwell's equation exactly by using a given particle distribution. These two approaches need to couple with a Fokker–Planck quasi-linear solver to address the wave absorption. Many important features of the LH wave propagation and absorption in tokamak have been successfully explained based on the linear and quasi-linear models. For example, the "spectral gap"[9] phenomena (referring to the difference of LH parallel refractive index between the launching location and absorption region) have been explained as the parallel spectrum up-shift and broadening effects due to the toroidicity and the wave diffraction. However, the nonlinear effects of the LH waves become increasingly important in tokamak plasmas with high heating power.[1] For example, the unsolved "density limit"[10] problem (referring to the decrease of current drive efficiency at higher plasma density) is believed to be related to the nonlinear parametric decay instability,[11] since the sideband waves have been observed in many experiments.[12–14]

Particle-in-cell (PIC) simulation approach is a powerful tool for studying nonlinear physics. Several PIC codes for radio frequency (RF) waves in the simple geometry (slab or cylinder) have been developed, e.g., GeFi,[15–17] Vorpal,[18,19] and G-gauge[20,21] codes. However, PIC simulations of RF waves had not been performed in the toroidal geometry before our earlier study of the LH wave propagation in tokamaks using a electrostatic PIC model.[22,23] In this work, we further develop a fully nonlinear electromagnetic PIC model, which has been successfully implemented into the gyrokinetic toroidal code (GTC).[24] This PIC model can address all the nonlinear physics associated with the LH waves, which includes the nonlinear particle trapping by the nonlinear wave–particle interaction and the parametric decay instability by the nonlinear wave–wave interaction. The electromagnetic dispersion relation and the nonlinear particle trapping of the LH waves have been verified in this paper. The nonlinear parametric decay instability of the LH waves will be reported in the future work.

In this paper, ion dynamics are described by the fluid equation for the study of the LH wave propagation and absorption. However, ion kinetic effects are important to the parametric decay instability of the LH waves. For example, nonlinear Landau damping by ions is important to some low frequency waves which are generated during the parametric decay instability.[12–14,25–28] In such cases, ion kinetic effects can be incorporated using 6D Vlasov equation, which has been implemented and verified in GTC.[22,29,30] Due to the fact that the LH wave frequency is much smaller than the electron cyclotron frequency $\omega \ll \Omega_{ce}$, and that the LH wavelength is much longer than the electron gyro-radius $k\rho_e \ll 1$, the electron dynamics are described by the drift kinetic (DK) equation using either kinetic momentum (symplectic formulation) or canonical momentum (Hamiltonian formulation). At the same time, the electron continuity equation is used for improving the numerical properties, which enforces the consistency between the perturbed density and the perturbed velocity. To study the LH wave dynamics in the core of tokamak plasmas, the light wave and parallel electron plasma wave are removed in order to relax the constraints on the spatial grid size and

a)Author to whom correspondence should be addressed. Electronic mail: zhihongl@uci.edu

time step size. The computational cost is expensive for the global simulation of LH waves in tokamak, since the LH wavelength is much shorter than the device size. For typical experimental parameters, the LH wave frequency is on the order of GHz, the parallel refractive index is around 1–2, the perpendicular wavelength is on the order of electron skin depth, and the parallel wavelength is on the order of ion skin depth. Thus, thousands of grids along radial, poloidal, and toroidal directions are required to resolve the short wavelength. In order to minimize the computational costs, we simulate the LH wave with one single toroidal wavelength and utilize the toroidal symmetry by only simulating $2\pi/n$ length of the toroidal angle, where $n$ is the toroidal mode number of the LH wave. This reduces the toroidal grid number from resolving hundreds of toroidal wavelengths to one toroidal wavelength. However, in the future study of parametric processes, where the toroidal mode numbers of the decay waves are usually smaller than the pump LH waves, the toroidal length of the simulation domain needs to be longer to resolve the waves with the lowest toroidal mode number. Furthermore, due to the fact that the mode structure of the LH wave is usually localized in tokamaks, we do not need many markers in the region where the LH wave amplitude is small. Thus, an importance sampling scheme is used in order to utilize the markers with high efficiency in PIC simulation.[31,32] The importance sampling scheme is a statistical technique which uses samples generated from a different distribution rather than the distribution of interest. In the importance sampling scheme, we load more markers in the region through which the LH wave will propagate and use the marker weight to represent the physical distribution. With these numerical techniques and simplifications on the physics model, computational costs are greatly reduced, while the important features relevant for current drive, such as LH wave propagation, mode conversion, and electron Landau damping, are still captured.

The nonlinear formulation for the LH wave is presented in Sec. II. The comparison of the analytic dispersion relation between the particle model and the full Maxwell model in the cold and uniform plasma limit is shown in Sec. III. The importance sampling PIC scheme for the LH wave simulation is shown in Sec. IV. The verifications of GTC simulations of the LH wave dispersion relation and nonlinear particle trapping are presented in Sec. V. We describe our conclusions in Sec. VI.

## II. NONLINEAR FORMULATION

When simulating LH wave propagation and absorption with negligible damping from ion species, ion dynamics are described by the fluid equation as described in Sec. II A. We use the drift kinetic equation to describe electron dynamics with two different guiding center formulations: the Hamiltonian formulation using canonical momentum and the symplectic formulation using kinetic momentum. These are described in Secs. II B and II C, respectively. Either of these formulations can be used to study the LH waves accurately. Poisson's equation and the electron perpendicular force balance equation are given in Sec. II D. In this paper, the notations $k_{||}$ and $k_{\perp}$ denote the parallel and perpendicular (with respect to the background magnetic field) wave vectors, respectively. $n_{||} = ck_{||}/\omega$ and $n_{\perp} = ck_{\perp}/\omega$ denote the parallel and perpendicular refractive index, respectively. $\omega_{pe}$ is the electron plasma frequency, $\omega_{pi}$ is the ion plasma frequency, $\Omega_{ce}$ is the electron cyclotron frequency, and $\Omega_{ci}$ is the ion cyclotron frequency.

### A. Fluid ions

The continuity and the momentum equations are used for describing the fluid ion dynamics:

$$\frac{\partial \delta n_i}{\partial t} + \nabla \cdot [(n_{i0} + \delta n_i)\boldsymbol{\delta u_i}] = 0, \tag{1}$$

$$m_i n_{i0} \frac{d\boldsymbol{\delta u_i}}{dt} = Z_i n_{i0}\left(\boldsymbol{\delta E} + \frac{1}{c}\boldsymbol{\delta u_i} \times \mathbf{B}\right) - \nabla \delta P_i, \tag{2}$$

where $\delta n_i$ and $\boldsymbol{\delta u_i}$ are the ion density and velocity perturbations, $\delta P_i \approx \delta n_i T_{i0}$ is the ion pressure perturbation, $n_{i0}$ and $T_{i0}$ are the ion equilibrium density and temperature, and $Z_i$ and $m_i$ are the ion charge and mass, respectively. $\boldsymbol{\delta E} = -\nabla\phi - \frac{1}{c}\frac{\partial \boldsymbol{\delta A}}{\partial t}$ is the perturbed electric field and $\mathbf{B} = \mathbf{B}_0 + \boldsymbol{\delta B}$ is the total magnetic field, where $\mathbf{B}_0 = \nabla \times \mathbf{A}_0$ is the equilibrium magnetic field, $\boldsymbol{\delta B} = \nabla \times \boldsymbol{\delta A}$ is the perturbed magnetic field, $\phi$ is the scalar potential, $\mathbf{A}_0$ is the equilibrium vector potential, and $\boldsymbol{\delta A}$ is the perturbed vector potential. In Eq. (2), $d/dt = \partial/\partial t + \boldsymbol{\delta u_i} \cdot \boldsymbol{\nabla}$ is the total time derivative which includes the convection term. For the LH wave simulation with $\omega \gg k_{\perp} v_{thi}$, we can drop the pressure term in Eq. (2), where $v_{thi} = \sqrt{2T_{i0}/m_i}$ is the ion thermal speed.

For computational convenience, we rewrite Eq. (2) into its canonical form by avoiding the calculation of $\partial \boldsymbol{\delta A}/\partial t$:

$$m_i n_{i0} \frac{d\boldsymbol{\delta U_i}}{dt} = -Z_i n_{i0} \nabla\left[\phi - \frac{1}{c}\boldsymbol{\delta u_i} \cdot (\mathbf{A}_0 + \boldsymbol{\delta A})\right], \tag{3}$$

where $\boldsymbol{\delta U_i} = \boldsymbol{\delta u_i} + \frac{Z_i}{cm_i}(\mathbf{A}_0 + \boldsymbol{\delta A})$ is the canonical velocity of the fluid ions. The total time derivative is defined as $d/dt = \partial/\partial t + \boldsymbol{\delta U_i} \cdot \boldsymbol{\nabla}$. Eq. (3) is used in the simulation instead of Eq. (2).

Furthermore, the 6D Vlasov equation has been adopted for describing fully kinetic ion dynamics in GTC and can be utilized when the ion kinetic effects are important.[22,29,30]

### B. Drift kinetic electron using canonical momentum

The Hamiltonian formulation using canonical momentum[33,34] is proposed to remove the $\partial \delta A_{||}/\partial t$ term in particle dynamic equations, which is difficult to implement as a time-centered finite difference in the simulation. In this section, we will introduce the formulation of the drift kinetic electron using canonical momentum in our model.

The nonlinear drift kinetic equation using canonical momentum for electrons is[33,34]

$$L_c f_e(\mathbf{X}, p_{||}, \mu, t) = 0, \tag{4}$$

where $f_e$ is the electron distribution function and $L_c$ is the propagator in canonical form, and $\mathbf{X}$, $p_{||}$, $\mu$ and $t$ denote the particle position, canonical momentum $m_e v_{||} + q_e \delta A_{||}/c$, magnetic moment and time, respectively.

The propagator $L_c$ consists of the equilibrium part $L_{c0}$, the first order perturbed part $\delta L_{c1}$, and the second order perturbed part $\delta L_{c2}$ as

$$L_{c0} = \frac{\partial}{\partial t} + \left(\frac{p_{||}}{m_e B_0}\mathbf{B}_0^{*\mathbf{c}} + \frac{c\mu}{q_e B_0}\mathbf{b}_0 \times \nabla B_0\right)\cdot\nabla - \frac{\mu}{B_0}\mathbf{B}_0^{*\mathbf{c}}\cdot\nabla B_0 \frac{\partial}{\partial p_{||}},$$

$$\delta L_{c1} = \left(-\frac{q_e \delta A_{||}}{c m_e}\frac{\mathbf{B}_0^{*\mathbf{c}}}{B_0} + \frac{c\mathbf{b}_0}{q_e B_0}\times q_e \nabla \Psi_l\right)\cdot\nabla - \frac{\mathbf{B}_0^{*\mathbf{c}}}{B_0}\cdot q_e \nabla \Psi_l \frac{\partial}{\partial p_{||}},$$

$$\delta L_{c2} = \frac{c\mathbf{b}_0}{q_e B_0}\times q_e \nabla \Psi_{nl}\cdot\nabla - \frac{\mathbf{B}_0^{*\mathbf{c}}}{B_0}\cdot q_e \nabla \Psi_{nl}\frac{\partial}{\partial p_{||}},$$

where $\mathbf{B}_0 = B_0\mathbf{b}_0$ is the equilibrium magnetic field, and $\mathbf{B}_0^{*\mathbf{c}} = \mathbf{B}_0 + \frac{c}{q_e}p_{||}\nabla\times\mathbf{b}_0$. The generalized potential consists of the linear and nonlinear parts $\Psi = \Psi_l + \Psi_{nl}$, where $\Psi_l = \phi - \frac{p_{||}\delta A_{||}}{m_e c} + \frac{\mu}{q_e}\delta B_{||}$ and $\Psi_{nl} = \frac{q_e \delta A_{||}^2}{2 m_e c^2}$. $\delta B_{||}$ and $\delta A_{||}$ are the compressional magnetic field perturbation and the parallel vector potential perturbation, respectively. The corresponding particle motion equations of Eq. (4) in magnetic coordinates are given in Appendix A.

The electron distribution function $f_e$ is also decomposed into the equilibrium and perturbed parts as $f_e = f_{e0} + \delta f_e$, and the equilibrium distribution function $f_{e0}$ satisfies the following equation:

$$L_{c0} f_{e0} = 0, \tag{5}$$

where we approximate $f_{e0}$ as a Maxwellian $f_{e0} = n_{e0}\left(\frac{m_e}{2\pi T_{e0}}\right)^{3/2} \times \exp\left(-\frac{p_{||}^2/m_e + 2\mu B}{2T_{e0}}\right)$ without the neoclassical correction, and the independent variable $p_{||}$ reduces to $p_{||} = m_e v_{||}$ in $f_{e0}$.

Considering Eq. (5), we can rewrite Eq. (4) as

$$\underbrace{L_{c0}\delta f_e + \delta L_{c1} f_{e0}}_{\{I\}} + \underbrace{\delta L_{c1}\delta f_e + \delta L_{c2} f_{e0}}_{\{II\}} + \underbrace{\delta L_{c2}\delta f_e}_{\{III\}} = 0, \tag{6}$$

where {I} represents the first order linear terms, {II} and {III} represent the second order and the third order nonlinear terms, respectively.

A perturbative $\delta f_e$ simulation method is applied to minimize the particle noise by defining the particle weight as $w_e = \delta f_e / f_e$, and the weight evolution equation can be written as

$$\frac{dw_e}{dt} = L_c w_e = \frac{1}{f_e} L_c \delta f_e = -\frac{1}{f_e}(\delta L_{c1} + \delta L_{c2}) f_{e0} = -(1 - w_e)\frac{1}{f_{e0}}(\delta L_{c1} + \delta L_{c2}) f_{e0}, \tag{7}$$

where Eq. (4) is used in deriving Eq. (7).

In principle, we can calculate both the density and parallel canonical velocity perturbations from the kinetic particles for calculating the perturbed fields. However, when we apply the $\delta f$ method and advance the weight equation by assuming $f_{e0} = f_{Maxwellian}$, the error $\Delta f = f_{\text{Marker}} - f_{Maxwellian}$ from the marker noise will accumulate in Eq. (7). Thus, after integrating the density and parallel canonical velocity perturbations from the marker distribution, the continuity equation will not be satisfied due to this error. The corresponding electrostatic potential and parallel vector potential will conflict with each other and cause numerical instabilities. This error can be reduced by increasing the marker number and will be eliminated when the marker number is infinite to build a perfect Maxwellian in the $\delta f$ simulation. In order to avoid this numerical issue, we use an additional electron continuity equation to time advance the electron density perturbation by the parallel canonical velocity perturbation calculated from the markers. The drift kinetic Eqs. (4) and (7) are only used for calculating the perturbed electron parallel canonical velocity and the perturbed pressure. This method provides much better consistency between the scalar potential and vector potential in the $\delta f$ simulation, since the continuity equation is satisfied all the time. The comparison of a single LH mode excitation between the cases with and without continuity equation is shown in Appendix B, which verifies the improved numerical properties using the continuity equation for the perturbed density.

Next, we integrate Eq. (6) to derive the electron continuity equation, and keep the leading linear and nonlinear terms based on the orderings: $u_{||e0} \approx 0$, $k_{||} \ll k_\perp$, $ck_\perp/\omega_{pe} \sim 1$, $\delta n_e/n_{e0} \sim \delta P_{||e}/P_{||e0} \sim \delta P_{\perp e}/P_{\perp e0} \sim \delta B_{||}/B_0 \sim |\boldsymbol{\delta}\mathbf{B}_\perp|/B_0$, $\nabla n_{e0}/n_{e0} \sim 1/a$, $\nabla T_{e0}/T_{e0} \sim 1/a$, $\nabla B_0/B_0 \sim 1/R$, $a/R < 1$. Then, we have

$$\underbrace{\frac{\partial \delta n_e}{\partial t} + \mathbf{B}_0\cdot\nabla\left[\frac{n_{e0}}{B_0}\left(\delta u_{||ec} - \frac{q_e\delta A_{||}}{m_e c}\right)\right]}_{\{I\}} \underbrace{+ B_0\mathbf{v}_\mathbf{E}\cdot\nabla\left(\frac{n_{e0}}{B_0}\right)}_{\{II\}} \underbrace{- n_{e0}(\mathbf{v}^* + \mathbf{v}_\mathbf{E})\cdot\frac{\nabla B_0}{B_0}}_{\{III\}} \underbrace{- \frac{c\mathbf{b}_0\times\nabla P_{\perp e0}}{q_e B_0}\cdot\frac{\nabla\delta B_{||}}{B_0}}_{\{IV\}}$$

$$\underbrace{+ B_0\mathbf{v}_\mathbf{E}\cdot\nabla\left(\frac{\delta n_e}{B_0}\right)}_{\{V\}} \underbrace{- \frac{c\mathbf{b}_0\times\nabla\delta P_{\perp e}}{q_e B_0}\cdot\frac{\nabla\delta B_{||}}{B_0}}_{\{VI\}} \underbrace{- \mathbf{B}_0\cdot\nabla\left(\frac{\delta n_e}{B_0}\frac{q_e\delta A_{||}}{m_e c}\right)}_{\{VII\}} \underbrace{+\nabla\times\left(\delta A_{||}\mathbf{b}_0\right)\cdot\nabla\left[\frac{n_{e0}}{B_0}\left(\delta u_{||ec} - \frac{q_e\delta A_{||}}{m_e c}\right)\right]}_{\{VIII\}} = 0, \tag{8}$$

where $\mathbf{v}_\mathbf{E} = \frac{c\mathbf{b}_0\times\nabla\phi}{B_0}$ is the $\mathbf{E}\times\mathbf{B}$ drift, $\mathbf{v}^* = \frac{\mathbf{b}_0\times\nabla\left(\delta P_{e\perp} + \delta P_{e||}\right)}{n_{e0} m_e \Omega_{ce}}$ is the diamagnetic drift, $\delta u_{||ec} = \frac{1}{n_{e0} m_e}\int \mathbf{dv} p_{||}\delta f_e$ is the canonical velocity, $\delta P_{||e} = \frac{1}{m_e}\int \mathbf{dv} p_{||}^2 \delta f_e$ and $\delta P_{\perp e} = \int \mathbf{dv}\mu B_0 \delta f_e$ are the parallel and perpendicular perturbed pressure, and $\int \mathbf{dv} = \frac{2\pi B_0}{m_e^2}\int dp_{||} d\mu$. The perpendicular equilibrium pressure in term {IV} is defined as $P_{\perp e0} = \int \mathbf{dv}\mu B_0 f_{e0} = n_{e0} T_{e0}$. The terms {I}–{IV} are linear, and the terms {V}–{VIII} are nonlinear. The term {I} is the linear parallel compressional term,

terms {II}–{IV} represent the linear work by the leading drifts, term {V} represents the $\mathbf{E}\times\mathbf{B}$ nonlinearity, term {VI} represents the diamagnetic drift nonlinearity, {VII} is the parallel nonlinear term, and {VIII} is the nonlinear magnetic compressional term.

Here, we use the parallel Ampere's law for solving $\delta A_{||}$ as

$$\left(\nabla_\perp^2-\frac{\omega_{pe}^2}{c^2}\right)\delta A_{||}=-\frac{4\pi}{c}\left(J_{||i}+J_{||e}\right), \tag{9}$$

where $J_{||i}=Z_i n_{i0}\delta u_{||i}$ and $J_{||e}=\frac{q_e}{m_e}\int \delta f_e p_{||}\mathbf{dv}$, $\delta u_{||i}$ is the parallel mechanical velocity of the fluid ions. The second term on the LHS of Eq. (9) arises due to the difference between $p_{||}$ and $m_e v_{||}$.

Inverting the Ampere's law (Eq. (9)), we have the relation: $\delta u_{||ec}-\frac{q_e\delta A_{||}}{m_e c}=-\frac{c}{4\pi n_{e0}q_e}\nabla_\perp^2\delta A_{||}+\delta u_{||i}$, which is used in terms {I} and {VIII} of Eq. (8) for better numerical stability.

### C. Drift kinetic electron using kinetic momentum

Although the drift kinetic equation using canonical momentum has some computational advantages, the drift kinetic equation using kinetic momentum (also called the symplectic formulation) is more transparent regarding the physical meaning of each term in the equations.[34] In this section, we introduce the drift kinetic equation using kinetic momentum as an alternative electron model.

Using guiding center position $\mathbf{X}$, parallel velocity $v_{||}$, and magnetic moment $\mu$ as independent variables in five dimensional phase space, the drift kinetic Vlasov equation for electrons is[34,35]

$$L_k f_e(\mathbf{X},v_{||},\mu,t)=0, \tag{10}$$

where $f_e(\mathbf{X},v_{||},\mu,t)$ is the electron distribution function and $L_k$ is the propagator in sympletic form. $L_k$ can be decomposed into the equilibrium part $L_{k0}$, the first order linear part $\delta L_{k1}$, and the second order nonlinear part $\delta L_{k2}$ as $L_k=L_{k0}+\delta L_{k1}+\delta L_{k2}$, with

$$L_{k0}=\frac{\partial}{\partial t}+\left(\frac{v_{||}}{B_0}\mathbf{B}_0^{*\mathbf{k}}+\frac{c\mathbf{b}_0}{q_e B_0}\times\mu\nabla B_0\right)\cdot\nabla-\frac{\mu}{m_e B_0}\mathbf{B}_0^{*\mathbf{k}}\cdot\nabla B_0\frac{\partial}{\partial v_{||}},$$

$$\delta L_{k1}=\left[v_{||}\frac{\boldsymbol{\delta}\mathbf{B}_\perp}{B_0}+\frac{c\mathbf{b}_0}{q_e B_0}\times\left(q_e\nabla\phi+\mu\nabla\delta B_{||}\right)\right]\cdot\nabla+\left[-\frac{\mu}{m_e B_0}\boldsymbol{\delta}\mathbf{B}_\perp\cdot\nabla B_0-\frac{\mathbf{B}_0^{*\mathbf{k}}}{m_e B_0}\cdot\left(q_e\nabla\phi+\mu\nabla\delta B_{||}\right)-\frac{q_e}{cm_e}\frac{\partial\delta A_{||}}{\partial t}\right]\frac{\partial}{\partial v_{||}},$$

$$\delta L_{k2}=-\frac{\boldsymbol{\delta}\mathbf{B}_\perp}{m_e B_0}\cdot\left(q_e\nabla\phi+\mu\nabla\delta B_{||}\right)\frac{\partial}{\partial v_{||}},$$

where $\mathbf{B}^{*\mathbf{k}}=\mathbf{B}_0^{*\mathbf{k}}+\boldsymbol{\delta}\mathbf{B}_\perp$, $\mathbf{B}_0^{*\mathbf{k}}=\mathbf{B}_0+\frac{B_0 v_{||}}{\Omega_{ce}}\nabla\times\mathbf{b}_0$, and $\boldsymbol{\delta}\mathbf{B}_\perp=\nabla_\perp\times(\delta A_{||}\mathbf{b}_0)$. The particle motion equations corresponding to Eq. (10) are given in Appendix A in magnetic coordinates.

Next, we will perform the same procedure as in Sec. II B to deduce the weight evolution equation and electron continuity equation. The distribution function is decomposed into the equilibrium and perturbed part as $f_e=f_{e0}+\delta f_e$. The equilibrium distribution $f_{e0}$ obeys the following equation:

$$L_{k0}f_{e0}=0, \tag{11}$$

where $f_{e0}$ is also approximated as a Maxwellian: $f_{e0}=n_{e0}(\frac{m_e}{2\pi T_{e0}})^{3/2}\exp(-\frac{m_e v_{||}^2+2\mu B}{2T_{e0}})$.

From Eqs. (10) and (11), we have

$$\underbrace{L_{k0}\delta f_e+\delta L_{k1}f_{e0}}_{\{I\}}+\underbrace{\delta L_{k1}\delta f_e+\delta L_{k2}f_{e0}}_{\{II\}}+\underbrace{\delta L_{k2}\delta f_e}_{\{III\}}=0, \tag{12}$$

where {I} represents the first order linear terms, {II} and {III} represent the second order and the third order nonlinear terms, respectively.

Defining the particle weight as $w_e=\delta f_e/f_e$, the weight evolution equation is

$$\begin{aligned}\frac{dw_e}{dt}&=L_k w_e=\frac{1}{f_e}L_k\delta f_e=-\frac{1}{f_e}(\delta L_{k1}+\delta L_{k2})f_{e0}\\&=-(1-w_e)\frac{1}{f_{e0}}(\delta L_{k1}+\delta L_{k2})f_{e0}.\end{aligned} \tag{13}$$

In the electron model with kinetic momentum, we also use the electron continuity equation for numerical stability as discussed in Sec. II B. Integrating Eq. (12) in velocity space and keeping the leading linear and nonlinear terms based on the same orderings in Sec. II B, we find that the electron continuity equation is given by

$$\begin{aligned}&\frac{\partial\delta n_e}{\partial t}\underbrace{+\mathbf{B}_0\cdot\nabla\left(\frac{n_{e0}\delta u_{||e}}{B_0}\right)}_{I}\underbrace{+B_0\mathbf{v}_\mathbf{E}\cdot\nabla\left(\frac{n_{e0}}{B_0}\right)}_{II}\underbrace{-n_{e0}(\mathbf{v}^*+\mathbf{v}_\mathbf{E})\cdot\frac{\nabla B_0}{B_0}}_{III}\underbrace{+\frac{c\mathbf{b}_0\times\nabla\delta B_{||}}{B_0^2}\cdot\frac{\nabla P_{\perp e0}}{q_e}}_{IV}\\&\underbrace{+\boldsymbol{\delta}\mathbf{B}_\perp\cdot\nabla\left(\frac{n_{e0}\delta u_{||e}}{B_0}\right)}_{V}\underbrace{+B_0\mathbf{v}_\mathbf{E}\cdot\nabla\left(\frac{\delta n_e}{B_0}\right)}_{VI}\underbrace{+\frac{c\mathbf{b}_0\times\nabla\delta B_{||}}{B_0^2}\cdot\frac{\nabla\delta P_{\perp e}}{q_e}}_{VII}=0,\end{aligned} \tag{14}$$

where $\delta u_{||e} = \frac{1}{n_{e0}} \int v_{||} \delta f_e \mathbf{dv}$ is the perturbed parallel velocity, $\delta P_{||e} = m_e \int \mathbf{dv} v_{||}^2 \delta f_e$ and $\delta P_{\perp e} = \int \mathbf{dv} \mu B_0 \delta f_e$ are the parallel and perpendicular perturbed pressures, $P_{\perp e0} = \int \mathbf{dv} \mu B_0 f_{e0} = n_{e0} T_{e0}$ is the perpendicular equilibrium pressure, $\mathbf{v_E} = \frac{c \mathbf{b}_0 \times \nabla \phi}{B_0}$ is the $\mathbf{E} \times \mathbf{B}$ drift velocity, $\mathbf{v}^* = \frac{\mathbf{b}_0 \times \nabla \left( \delta P_{\perp e} + \delta P_{||e} \right)}{n_{e0} m_e \Omega_{ce}}$ is the perturbed diamagnetic drift velocity, and $\int \mathbf{dv} = \frac{2\pi B_0}{m_e} \int dv_{||} d\mu$. The terms related to $\delta B_{||}$ in Eq. (14) are the diamagnetic drift due to the parallel perturbed magnetic field, and the other terms are the same as in Eq. (28) in Ref. 36. In Eq. (14), the terms {I}–{IV} are linear while the terms {V}–{VII} are nonlinear.

In order to calculate $\partial \delta A_{||} / \partial t$ value for pushing the particles, we first take the time derivative of the parallel Ampere's law as

$$\nabla_\perp^2 \frac{\partial \delta A_{||}}{\partial t} = -\frac{4\pi}{c} \left( Z_i n_{i0} \frac{\partial \delta u_{||i}}{\partial t} + q_e n_{e0} \frac{\partial \delta u_{||e}}{\partial t} \right). \tag{15}$$

Second, we integrate Eq. (12) to get the momentum equation based on the same ordering with Eq. (14) as

$$\begin{aligned} & n_{e0} \frac{\partial \delta u_{||e}}{\partial t} \underbrace{+ \frac{q_e n_{e0}}{m_e} \mathbf{b}_0 \cdot \nabla \phi}_{I} + \underbrace{\frac{q_e n_{e0}}{m_e c} \frac{\partial \delta A_{||}}{\partial t}}_{II} + \underbrace{\frac{B_0}{m_e} \mathbf{b}_0 \cdot \nabla \left( \frac{\delta P_{||e}}{B_0} \right)}_{III} + \underbrace{\frac{\mathbf{B}_0 \cdot \nabla \delta B_{||}}{m_e B_0^2} P_{\perp e0}}_{IV} \\ & \underbrace{+ \frac{q_e \delta n_e}{m_e} \mathbf{b}_0 \cdot \nabla \phi}_{V} + \underbrace{\frac{q_e \delta n_e}{m_e c} \frac{\partial \delta A_{||}}{\partial t}}_{VI} + \underbrace{\frac{q_e n_{e0}}{m_e B_0} \boldsymbol{\delta} \mathbf{B}_\perp \cdot \nabla \phi}_{VII} + \underbrace{\frac{\boldsymbol{\delta} \mathbf{B}_\perp}{m_e} \cdot \nabla \left( \frac{\delta P_{||e}}{B_0} \right)}_{VIII} \underbrace{+ B_0 \mathbf{v_E} \cdot \nabla \left( \frac{n_{e0} \delta u_{||e}}{B_0} \right)}_{IX} = 0, \end{aligned} \tag{16}$$

where terms {I}–{IV} are linear and {V}–{IX} are nonlinear in Eq. (16).

Third, we calculate $\partial \delta u_{||i} / \partial t$ from Eq. (2) as

$$\frac{\partial \delta u_{||i}}{\partial t} = \frac{Z_i}{m_i} \left( -\mathbf{b}_0 \cdot \nabla \phi - \frac{1}{c} \frac{\partial \delta A_{||}}{\partial t} \right). \tag{17}$$

Substituting Eqs. (16) and (17) into Eq. (15), we can derive the following equation for $\partial \delta A_{||} / \partial t$:

$$\left( \nabla_\perp^2 - \frac{\omega_{pe}^2}{c^2} - \frac{\omega_{pi}^2}{c^2} \right) \frac{\partial \delta A_{||}}{\partial t} = \frac{\omega_{pe}^2}{c^2} \xi_{||}, \tag{18}$$

where

$$\begin{aligned} \xi_{||} = & c \left( 1 + \frac{m_e}{m_i} \right) \mathbf{b}_0 \cdot \nabla \phi + \frac{c}{n_{e0} q_e} \mathbf{B}_0 \cdot \nabla \left( \frac{\delta P_{||e}}{B_0} \right) \\ & + \frac{c}{n_{e0} q_e} \frac{\mathbf{B}_0 \cdot \nabla \delta B_{||}}{B_0^2} P_{\perp e0} + c \frac{\delta n_e}{n_{e0}} \mathbf{b}_0 \cdot \nabla \phi \\ & + \frac{c}{B_0} \boldsymbol{\delta} \mathbf{B}_\perp \cdot \nabla \phi + \frac{c}{n_{e0} q_e} \boldsymbol{\delta} \mathbf{B}_\perp \cdot \nabla \left( \frac{\delta P_{||e}}{B_0} \right) \\ & + \frac{c m_e B_0}{n_{e0} q_e} \mathbf{v_E} \cdot \nabla \left( \frac{n_{e0} \delta u_{||e}}{B_0} \right) + \frac{\delta n_e}{n_{e0}} \frac{\partial \delta A_{||}}{\partial t}. \end{aligned}$$

Eq. (18) with nonlinear terms is solved by an iterative method: we solve it without the last term in $\xi_{||}$, then substitute the result of $\partial \delta A_{||} / \partial t$ into $\xi_{||}$, and solve Eq. (18) again to get the new $\partial \delta A_{||} / \partial t$. One iteration is enough for convergence since the last term $(\delta n_e / n_{e0})(\partial \delta A_{||} / \partial t)$ is much smaller than the other terms in $\xi_{||}$.

Alternatively, we could move $(\delta n_e / n_{e0})(\partial \delta A_{||} / \partial t)$ in $\xi_{||}$ to the LHS of Eq. (18), and solve $\partial \delta A_{||} / \partial t$ directly without iteration. However, this requires initializing the matrix $\nabla_\perp^2 - \frac{\omega_{pe}^2}{c^2} - \frac{\omega_{pi}^2}{c^2} - \frac{\delta \omega_{pe}^2}{c^2}$ (where $\delta \omega_{pe}^2 = \frac{4\pi \delta n_e e^2}{m_e}$) using the PETSc software at each time step in the simulation, which will slow down the computational speed.

In Secs. II B and II C, electron models using canonical momentum (Hamiltonian formulation) and kinetic momentum (symplectic formulation) have been discussed. Both of them apply the continuity equation to avoid numerical instability. The leading terms of the continuity equations from these two models are the same except for an additional term {VII} in Eq. (8), which is due to the difference between $p_{||}$ and $v_{||}$ as independent variables of these two models. However, the different term is very small compared to the sum of the other terms, and either of these two models can be applied to the simulations.

### D. Field equations

The Poisson's equation for fluid (or fully kinetic) ions and drift kinetic electrons is[34,37]

$$\begin{aligned} & \nabla_\perp^2 \phi \underbrace{+ \nabla_\perp \cdot \left( \frac{\omega_{pe}^2}{\Omega_{ce}^2} \nabla_\perp \phi \right)}_{I} \\ & = -4\pi (Z_i \delta n_i + q_e \delta n_e) + 4\pi \nabla_\perp \cdot \\ & \quad \times \left( \underbrace{\frac{q_e n_{e0}}{B_0^2} \mathbf{B}_0 \times \boldsymbol{\delta} \mathbf{A}_\perp}_{II} + \underbrace{\frac{c m_e n_{e0} u_{||e0}}{B_0^2} \nabla_\perp \delta A_{||}}_{III} \right). \end{aligned} \tag{19}$$

In Eq. (19), the parallel electron plasma wave is suppressed by assuming $\nabla^2 \approx \nabla_\perp^2$ in the first term on the LHS. Term {I} is the electron density perturbation caused by the polarization drift, term {II} is the density perturbation caused by the electron $\mathbf{E} \times \mathbf{B}$ drift due to the inductive electric field $\partial \boldsymbol{\delta} \mathbf{A}_\perp / \partial t$, term {III} is the electron density perturbation caused by the magnetic-flutter motion along perturbed magnetic-field lines, and $u_{||e0} = (1/n_{e0}) \int v_{||} f_{e0} \mathbf{dv}$ is the electron equilibrium flow.

In the LH wave frequency range $\omega \ll \Omega_{ce}$, we can use the electron perpendicular force balance equation to solve $\delta B_{||}$ and $\phi$ together with Eq. (19), which is given as follows:

$$n_e q_e \boldsymbol{\delta}\mathbf{E}_\perp = \nabla_\perp \cdot \boldsymbol{\delta}\mathbf{P_e} - \frac{1}{c}\mathbf{J}_{e\perp} \times \mathbf{B}_0, \tag{20}$$

where the perpendicular electric field $\boldsymbol{\delta}\mathbf{E}_\perp$ is defined as

$$\boldsymbol{\delta}\mathbf{E}_\perp = -\nabla_\perp \phi - \frac{1}{c}\frac{\partial \boldsymbol{\delta}\mathbf{A}_\perp}{\partial t}, \tag{21}$$

the divergence of the electron pressure is

$$\nabla_\perp \cdot \boldsymbol{\delta}\mathbf{P_e} \approx \nabla_\perp \left( \delta P_{\perp e} + \frac{n_{e0} T_{e0} \delta B_{||}}{B_0} \right), \tag{22}$$

and the electron perpendicular current is

$$\mathbf{J_{e\perp}} \approx \frac{c}{4\pi}\left[\nabla_\perp \delta B_{||} \times \mathbf{b}_0 + \nabla_{||} \times \left(\nabla_\perp \delta A_{||} \times \mathbf{b}_0\right)\right] - \mathbf{J_{i\perp}}. \tag{23}$$

In Eq. (22), we neglect the electron polarization drift $\mathbf{v_{pol}} = (q_e/m_e\Omega_{ce}^2)(\partial \boldsymbol{\delta}\mathbf{E}_\perp/\partial t)$ contribution to the pressure term based on the drift kinetic electron assumption (the electron Larmor radius is much smaller than the perpendicular wavelength $k_\perp \rho_e \ll 1$), since the pressure caused by the polarization drift is $\delta P_{pol} \approx \delta n_{pol} T_{e0} = q_e n_{e0} \rho_e^2 \nabla_\perp^2 \phi \approx 0$. The first term on the RHS of Eq. (22) is calculated from the guiding center dynamics, and the second term on the RHS is the pressure perturbation caused by the electron $\mathbf{E} \times \mathbf{B}$ drift due to the inductive electric field $\partial \boldsymbol{\delta}\mathbf{A}_\perp/\partial t$, which does not appear in the guiding center dynamic equation explicitly.

Taking the perpendicular divergence operation on both sides of Eq. (20), we have

$$\begin{aligned} -\nabla_\perp^2 \phi + \frac{1}{c}\mathbf{b}_0 \cdot \nabla \frac{\partial \delta A_{||}}{\partial t} &= \nabla_\perp \cdot \left[ \frac{1}{n_{e0} q_e} \nabla_\perp \left( \delta P_{\perp e} + \frac{n_{e0} T_{e0} \delta B_{||}}{B_0} \right) \right] \\ &+ \nabla_\perp \cdot \left( \frac{B_0}{4\pi n_{e0} q_e} \nabla_\perp \delta B_{||} \right) + \frac{1}{n_{e0} q_e c} \nabla_\perp \cdot (\mathbf{J_{i\perp}} \times \mathbf{B}_0). \end{aligned} \tag{24}$$

Although in the LH frequency range, we have $|\mathbf{J_{i\perp}}|/|\mathbf{J}_{e\perp}| \approx (m_e/m_i)(\Omega_{ce}/\omega_{LH}) \ll 1$, where $\omega_{LH} \approx \sqrt{\Omega_{ce}\Omega_{ci}}$, we keep $\mathbf{J_{i\perp}}$ related terms in Eq. (24) to extend the simulation to the lower frequency range $\omega \ll \omega_{LH}$. The second term on the LHS of Eq. (24) is from the time derivative of the Coulomb gauge: $\nabla_\perp \cdot (\partial \boldsymbol{\delta}\mathbf{A}_\perp/\partial t) = -\mathbf{b}_0 \cdot \nabla(\partial \delta A_{||}/\partial t)$, which is much smaller than the first term on the LHS in the LH wave simulation and, thus, can be dropped.

In the multi-pass cases, when the LH wave propagates to the edge region, the reflections will happen at the cutoffs, where $\omega = \omega_{pe}$, and the perpendicular refractive index $n_\perp$ will decrease to zero very quickly. Thus, due to the fact that the equilibrium density scale length is comparable to the wave length (i.e., $k_\perp L_n \sim 1$) near the cutoffs in the edge region, the terms related to the non-uniformity of the equilibrium need to be kept in Eqs. (19) and (24). However, the cutoff region with $\omega = \omega_{pe}$ is removed in this model using the approximation $\nabla^2 \approx \nabla_\perp^2$ to the first term on the LHS of Eq. (19). Thus, this model cannot address the reflection of the LH waves at the cutoffs. In this paper, we focus on the single-pass study of the LH wave in the core plasmas, where most of the LH wave energy can be absorbed before reaching the cutoffs near the plasma edge. In the core plasmas, the wavelength of the LH wave is much smaller than the equilibrium plasma scale length $L_0 \sim (L_n = 2\pi n_{e0}/\nabla n_{e0}, L_T = 2\pi T_{e0}/\nabla T_{e0}, L_B = 2\pi B_0/\nabla B_0)$, namely, $k_\perp L_0 \gg 1$ can be guaranteed during the simulation. Furthermore, we can assume the electron equilibrium flow $u_{||e0} = 0$ for a Maxwellian distribution of the electrons. Thus, we can simplify Eqs. (19) and (24) as

$$\left(1 + \frac{\omega_{pe}^2}{\Omega_{ce}^2}\right)\nabla_\perp^2 \phi + \frac{4\pi n_{e0} q_e}{B_0} \delta B_{||} = -4\pi (Z_i \delta n_i + q_e \delta n_e), \tag{25}$$

and

$$\delta B_{||} = \frac{4\pi}{B_0(1 + 0.5\beta_e)}(n_{e0} q_e \chi - n_{e0} q_e \phi - \delta P_{\perp e}), \tag{26}$$

where $\beta_e = 8\pi n_{e0} T_{e0}/B_0^2$, and $\chi$ can be derived from the following equation:

$$\nabla_\perp^2 \chi = -\frac{1}{n_{e0} q_e c} \nabla_\perp \cdot (\mathbf{J_{i\perp}} \times \mathbf{B}_0). \tag{27}$$

Here, we notice that in the fluid ion (or fully kinetic ion[15]) and DK electron model, the force balance Eq. (26) for $\delta B_{||}$ is different from the one in the gyrokinetic (GK) ion and DK electron model (i.e., $4\pi(\delta P_{i\perp} + \delta P_{e\perp}) + (1 + \beta_e + \beta_i)\delta B_{||} B_0 = 0$ in the lowest order).[34,35] This is due to the fact that the electron $\mathbf{E} \times \mathbf{B}$ drift motion cannot cancel with ion species in the LH frequency range in our model. Substituting Eq. (26) into Eq. (25), we can solve the following equation to derive $\phi$:

$$\begin{aligned} \left(1 + \frac{\omega_{pe}^2}{\Omega_{ce}^2}\right)\nabla_\perp^2 \phi - \frac{\omega_{pe}^2}{\Omega_{ce}^2}\frac{\omega_{pe}^2}{c^2}\frac{\phi}{1 + 0.5\beta_e} &= -4\pi \left[ Z_i \delta n_i + q_e \delta n_e - q_e \frac{\beta_e}{(2 + \beta_e)} \frac{\delta P_{\perp e}}{T_{e0}} \right] \\ &- \frac{\omega_{pe}^2}{\Omega_{ce}^2}\frac{\omega_{pe}^2}{c^2}\frac{\chi}{1 + 0.5\beta_e}. \end{aligned} \tag{28}$$

$\boldsymbol{\delta}\mathbf{A}_\perp$ can be solved from

$$\nabla_\perp^2 \boldsymbol{\delta}\mathbf{A}_\perp = -\nabla_\perp \delta B_{||} \times \mathbf{b}_0. \tag{29}$$

Now, Eqs. (1), (3)–(4), (7)–(9), and (26)–(29) form a closed system for the electron model using canonical momentum, while Eqs. (1), (3), (10), (13)–(14), (18), and (26)–(29) form a closed system for the electron model using kinetic momentum. In linear and nonlinear regimes, electron models using either kinetic or canonical momentum can be applied to the LH wave studies with the similar complexity and numerical performance.

## III. ANALYTIC DISPERSION RELATION FROM ELECTROMAGNETIC PARTICLE MODEL

In order to verify the validity of the electromagnetic models given in Sec. II, we derive the corresponding linear dispersion relation and compare it with the result from the Maxwell equations in the limit of uniform and cold plasmas.

We start from the electron model using kinetic momentum, using Eqs. (1), (3), (10), (13)–(14), (18), and (26)–(29).

In the cold and uniform plasmas, Eq. (18) reduces to

$$\left(\nabla_\perp^2 - \frac{\omega_{pe}^2}{c^2} - \frac{\omega_{pi}^2}{c^2}\right)\frac{\partial \delta A_{||}}{\partial t} = \frac{\omega_{pe}^2}{c}\left(1 + \frac{m_e}{m_i}\right)\mathbf{b}_0 \cdot \nabla\phi. \quad (30)$$

Eq. (26) reduces to

$$\delta B_{||} = -\frac{\omega_{pe}^2}{\Omega_{ce} c}(\phi - \chi), \quad (31)$$

and Eq. (28) reduces to

$$\left(1 + \frac{\omega_{pe}^2}{\Omega_{ce}^2}\right)\nabla_\perp^2\phi - \frac{\omega_{pe}^2}{\Omega_{ce}^2}\frac{\omega_{pe}^2}{c^2}\phi = -4\pi(Z_i\delta n_i + q_e\delta n_e) - \frac{\omega_{pe}^2}{\Omega_{ce}^2}\frac{\omega_{pe}^2}{c^2}\chi. \quad (32)$$

The ion dynamics are described by Eq. (3) in canonical form, which has the numerical advantage by avoiding the calculation of $\partial\delta\mathbf{A}/\partial t$. For the convenience of theoretical analysis, we use the equivalent Eq. (2) in the cold plasma limit, and decompose the ion perturbed velocity into parallel and perpendicular components

$$\delta u_{i||} = \frac{iZ_i}{m_i\omega}\delta E_{||}, \quad (33)$$

and

$$\delta\mathbf{u}_{\mathbf{i}\perp} = \frac{iZ_i\omega}{m_i\left(\omega^2 - \Omega_{ci}^2\right)}\left[\delta\mathbf{E}_\perp + \frac{i\Omega_{ci}}{\omega}\delta\mathbf{E}_\perp \times \mathbf{b}_0\right]. \quad (34)$$

After linearization, the ion continuity Eq. (1) in uniform plasmas can be written as

$$\frac{\partial\delta n_i}{\partial t} + n_{i0}\nabla\cdot\delta\mathbf{u}_\mathbf{i} = 0. \quad (35)$$

The electron dynamics are described by the continuity equation and drift kinetic equation. In the uniform and cold plasmas, the electron continuity Eq. (14) reduces to

$$\frac{\partial\delta n_e}{\partial t} + n_{e0}\mathbf{b}_0\cdot\nabla\delta u_{e||} = 0. \quad (36)$$

Integrating Eq. (12) (equivalent to Eqs. (10) and (13)) for the momentum moment and keeping the linear terms in the cold and uniform plasma, we have

$$\frac{\partial\delta u_{e||}}{\partial t} + \frac{q_e}{m_e}\mathbf{b}_0\cdot\nabla\phi + \frac{q_e}{m_e c}\frac{\partial\delta A_{||}}{\partial t} = 0. \quad (37)$$

Applying the Fourier transform to Eqs. (30)–(37): $\partial_t \to -i\omega$, $\mathbf{b}_0\cdot\nabla \to ik_{||}$, and $\nabla_\perp \to i\mathbf{k}_\perp$, we can derive the linear dispersion relation in the cold and uniform plasmas as

$$S + D^2\frac{1}{n_\perp^2 - S'} = -(P-1)\frac{n_{||}^2}{n_\perp^2 - (P-1)}, \quad (38)$$

where $S$, $P$, and $D$ are the elements of the cold plasma dielectric tensor in Stix notation with frequency $\omega \ll \Omega_{ce}$ as follows:

$$S = 1 + \frac{\omega_{pe}^2}{\Omega_{ce}^2} - \frac{\omega_{pi}^2}{\omega^2 - \Omega_{ci}^2},$$

$$P = 1 - \frac{\omega_{pe}^2}{\omega^2} - \frac{\omega_{pi}^2}{\omega^2},$$

$$D = -\frac{\omega_{pe}^2}{\omega\Omega_{ce}} + \frac{\omega_{pi}^2\Omega_{ci}}{\omega\left(\omega^2 - \Omega_{ci}^2\right)}.$$

$S'$ in Eq. (38) is given as

$$S' = S - 1 - \frac{\omega_{pe}^2}{\Omega_{ce}^2} = -\frac{\omega_{pi}^2}{\omega^2 - \Omega_{ci}^2}.$$

Although the dispersion relation in Eq. (38) was derived using the electron model with kinetic momentum, it can also be derived from the canonical momentum model, using Eqs. (1), (3)–(4), (7)–(9), and (26)–(29).

We rewrite Eq. (38) into the determinant form and compare it with the well-known result from the Maxwell model[38] in Table I.

Compared to the Maxwell model solution, the difference in $S'$ of our reduced model is due to the fact that we drop the displacement and polarization currents in the perpendicular electron force balance equation. The vacuum term is lost in the parallel diagonal term $P - 1 - n_\perp^2$ of the reduced model, since we remove the electron plasma wave by dropping the $\nabla_{||}^2\phi$ term in Poisson's equation, and remove the light wave by dropping the displacement current in the parallel Ampere's law. The missing $-n_{||}^2$ in the second diagonal term of the reduced model is due to the fact that we assume $|\nabla_\perp| \gg |\nabla_{||}|$ in the parallel Ampere's law and the perpendicular force balance equation, and drop some coupling terms between the parallel and perpendicular wave vectors.

Thus, our simulation model is accurate for the waves in the core region of a typical tokamak where the plasma density is high, such that $\omega \ll \omega_{pe}$ or $|P| \gg 1$ and the LH wave's perpendicular refractive index is much larger than the parallel refractive index $(n_\perp^2 \gg n_{||}^2)$. Namely, our

TABLE I. Analytic dispersion relations derived from the reduced model and the Maxwell model, respectively.

| Reduced model solution | Maxwell model solution |
|---|---|
| $\begin{vmatrix} S - n_{||}^2 & -iD & n_{||}n_\perp \\ iD & S' - n_\perp^2 & 0 \\ n_{||}n_\perp & 0 & P - 1 - n_\perp^2 \end{vmatrix} = 0$ | $\begin{vmatrix} S - n_{||}^2 & -iD & n_{||}n_\perp \\ iD & S - n_\perp^2 - n_{||}^2 & 0 \\ n_{||}n_\perp & 0 & P - n_\perp^2 \end{vmatrix} = 0$ |

simulation results can recover the results of the Maxwell model when $|S' - n_\perp^2| \gg |1 + \omega_{pe}^2/\Omega_{ce}^2 - n_\parallel^2|$ and $|P| \gg 1$ are satisfied simultaneously. The high frequency light wave and electron plasma wave are artificially removed, enabling us to use a larger spatial grid size and time step size in the simulation by not resolving the high frequency and short wavelength waves. This is efficient and sufficient for the case of single-pass absorption of LH waves without cutoff. However, our simulation fails when the LH waves propagate to the cutoff layer in the plasma edge where $n_\perp^2 \sim 0$, and the electron plasma wave and light wave cannot be ignored. Thus, in order to address the multi-pass physics accurately, this field model for the core plasma needs to couple with the Maxwell model at the edge plasma.

## IV. IMPORTANCE SAMPLING FOR PARTICLE-IN-CELL SIMULATION

In order to efficiently reduce the numerical noise and the computational cost in marker particle simulation, it is helpful to load many markers at the initial time in the region through which the LH wave will propagate, while loading a very small number of markers in the region where LH wave perturbations are small. Thus, the importance sampling scheme[31,32] is applied to PIC simulation of LH waves. Here, we give an example of this scheme based on the electron model using canonical momentum.

The marker distribution is defined as $g_e(\mathbf{X}, p_\parallel, \mu, t) = g_{e0}(\mathbf{X}, p_\parallel, \mu) + \delta g_e(\mathbf{X}, p_\parallel, \mu, t)$, where $g_{e0} = g_e(t = 0)$ is the initial sampling marker distribution, and $\delta g_e$ is the perturbed marker distribution.

Similar to Eq. (4), the drift kinetic equation for marker distribution can be written as

$$L_c g_e = (L_{c0} + \delta L_{c1} + \delta L_{c2})(g_{e0} + \delta g_e) = 0. \tag{39}$$

Instead of a single weight as defined in Sec. II, two weights are used in the importance sampling scheme. The total weight is defined as

$$p_e = \frac{f_e}{g_e}, \tag{40}$$

which represents the importance of each marker to $f_e$. The perturbed weight is defined as

$$w_e = \frac{\delta f_e}{g_e}, \tag{41}$$

which represents the importance of each marker to $\delta f_e$.

Thus, considering Eqs. (4), (6) and (39), the total weight evolution equation is

$$\frac{dp_e}{dt} = 0, \tag{42}$$

and the perturbed weight evolution equation becomes:

$$\frac{dw_e}{dt} = -(p_e - w_e)\frac{1}{f_{e0}}(\delta L_{c1} + \delta L_{c2}) f_{e0}. \tag{43}$$

Eqs. (42) and (43) determine the evolution of the total distribution $f_e$ and the perturbed distribution $\delta f_e$, respectively. Because the marker distribution does not need to be proportional to the physical distribution in the importance sampling scheme: $g_e \neq C \cdot f_e$, where $C$ is a constant, we need to evolve Eqs. (42) and (43) while considering the importance of the markers. Furthermore, we can also apply this scheme to the electron model using kinetic momentum by replacing $\delta L_{c1} + \delta L_{c2}$ with $\delta L_{k1} + \delta L_{k2}$ in Eq. (43).

In principle, we can sample arbitrary $g_{e0}(\mathbf{X}, p_\parallel, \mu)$ initially in order to achieve local high resolution in the phase space, where the $\delta f$ amplitude is high. For the phase space volume conservation as shown in Eq. (39), the perturbed marker distribution will evolve through the following equation:

$$L_c \delta g_e = -(\delta L_{c1} + \delta L_{c2}) g_{e0} - L_{c0} g_{e0}. \tag{44}$$

The reason why we keep the last term on the RHS of Eq. (44) is that $L_{c0} g_{e0} \neq 0$, in general, when we choose an approximate $g_{e0}$ for optimal phase space sampling. Finite $\delta g_e$ makes $g_e$ different from the initial arrangement $g_{e0}$ and changes the desired numerical resolution. However, the time scale for the marker evolution is much longer than the LH wave period $|L_c \delta g_e / \delta g_e| \ll \omega_{\mathrm{LH}}$. Thus, the desired numerical resolution does not vary much for the duration of the LH wave simulation.

The general magnetic flux coordinates system $(\psi, \theta, \zeta)$ is used for the simulations of LH waves in toroidal geometry, where $\psi$ is the poloidal flux function, $\theta$ is the magnetic poloidal angle, and $\zeta$ is the magnetic toroidal angle. For the simulation of LH waves launched from $\theta = 0$, we sample many markers in the region of LH wave propagation, as shown in Fig. 1. The coordinates (X, Z) in Figs. 1, 2(a), and 2(d) represent the horizontal and vertical distances measured from the geometric center of the tokamak, and the color scale in Fig. 1 represents the number of the markers per cell used in the simulation. In the simulation, the axis values of the electron plasma temperature and the plasma density are $T_{e0} = 1.0\,\mathrm{keV}$ and

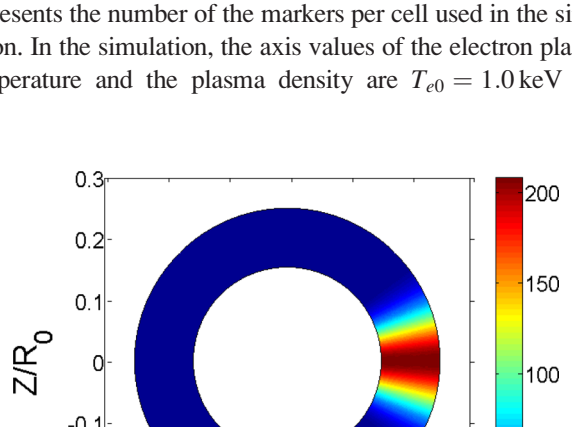


FIG. 1. Marker distribution of the importance sampling in the real space, which is used in the simulation of the LH wave propagation. The color scale represents the number of the markers per cell.

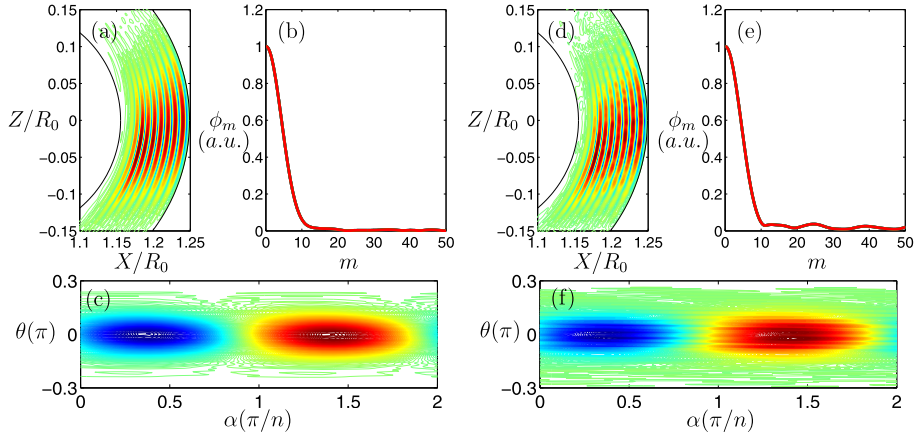


FIG. 2. Panels (a)–(c) are from the importance sampling PIC simulation, which show the LH wave structure in the poloidal plane, the poloidal spectrum of the wave-packet, and the LH wave structure on the flux-surface, respectively. Panels (d)–(f) are from the simulation with uniform sampling. The color scales in panels (a), (c), (d), and (f) represent the electrostatic potential $\phi$ in arbitrary units. $m$ is the poloidal harmonic number in panels (b) and (e). The mode structures in the importance sampling case as shown by (a) and (c) are much smoother than in the uniform sampling as shown by (d) and (f). The amplitudes of the numerical high $m$ harmonics in the importance sampling (b) are much smaller than in the uniform sampling (e).

$n_{i0} = n_{e0} = 5.0 \times 10^{13}\,\mathrm{cm}^{-3}$, respectively. We choose the other parameters based on the orders of magnitude of the Alcator C-mod tokamak, which includes $a = 0.16\,\mathrm{m}$, $R_0 = 0.64\,\mathrm{m}$, and the axis value of the magnetic field $B_a = 5.0\,\mathrm{T}$. The launched LH wave frequency is $f_0 = 4.6\,\mathrm{GHz}$ and the toroidal refractive index is $n_t = ck_t/\omega = 1.86$. The comparison of the numerical performance between the uniform sampling and importance sampling is shown in Fig. 2. We find that the mode structures in the poloidal plane and flux-surface with importance sampling are much smoother than with uniform sampling. The horizontal coordinate $\alpha = \theta - \zeta/q$ in Figs. 2(c) and 2(f) is the magnetic field line label. The horizontal coordinate $m$ is the poloidal mode number in Figs. 2(b) and 2(e). The high $m$ poloidal components of the wave-packet are nearly zero in the importance sampling case as shown in Fig. 2(b), while the high $m$ poloidal components of the wave-packet have larger amplitudes in the uniform sampling case as shown in Fig. 2(e), which proves that the importance sampling PIC method helps to decrease the numerical noise and suppress the numerical high $k_\theta$ modes.

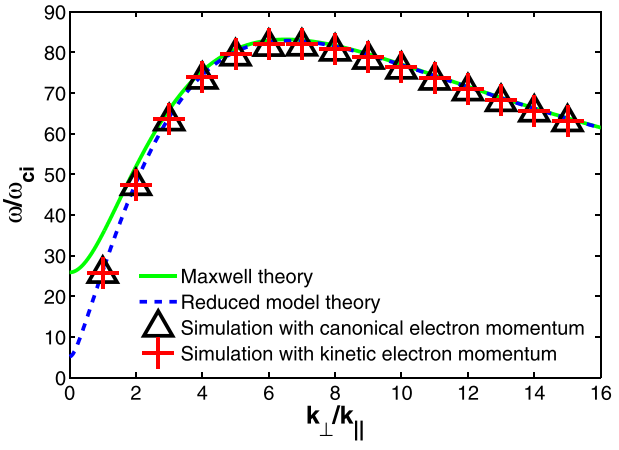


FIG. 3. Comparison of the electromagnetic dispersion relation of the LH waves between GTC simulation and the theory.

## V. VERIFICATION OF GTC SIMULATION OF DISPERSION RELATION AND NONLINEAR PARTICLE TRAPPING OF LH WAVES

In this section, we will show the benchmark of the LH wave dispersion relation between the simulation and the theory. The model described in Sec. II has been implemented in the gyrokinetic toroidal code (GTC). GTC[24,39] has been successfully applied to simulate microturbulence,[40] energetic particle transport,[41] Alfven eigenmodes,[42,43] and magneto-hydrodynamic instabilities including kink mode[44] and tearing mode[45] in fusion plasmas. In order to benchmark against the theoretical solution, the simulations are performed in the cylinder geometry of GTC with uniform magnetic field in this section. For these benchmark cases, plasma density $n_{e0} = n_{i0} = 2 \times 10^{13}\,\mathrm{cm}^{-3}$, electron temperature $T_{e0} = 50.0\,\mathrm{eV}$ (for cold plasma), and magnetic field $B = 2.0\,\mathrm{T}$ are uniform, and the magnetic field is only along the axial direction in the cylinder. The parallel LH wave vector in the simulation is fixed as $k_{||} = n/R = 100.0\,\mathrm{m}^{-1}$, where $n = 100$ is the parallel mode number and $R = 1.0\,\mathrm{m}$ (the length of the cylinder is $l = 2\pi R$), and the radius is $a = 0.3\,\mathrm{m}$. GTC simulations of LH waves in different $k_\perp/k_{||}$ regimes are carried out by varying the perpendicular wave vector $k_\perp$. In the simulation, we perturb the electron density at the initial time, then allow the perturbation to evolve self-consistently, and measure the oscillation frequency of the perturbed fields. This method is known as the initial perturbation method.[46,47] The simulations are carried out using both electron models, and the comparison between the simulations and the theory is shown in Fig. 3. It is seen that there are two branches of waves in Fig. 3: the slow wave and the fast wave. The perpendicular phase velocity $v_{p\perp} = \omega/k_\perp$ and group velocity $v_{g\perp} = \partial\omega/\partial k_\perp$ have the same sign for the fast wave, which corresponds to the left part of the dispersion relation curve in Fig. 3; while they have opposite signs for the slow wave, which corresponds to the right part of the dispersion relation curve in Fig. 3. Simulation results agree with the analytic

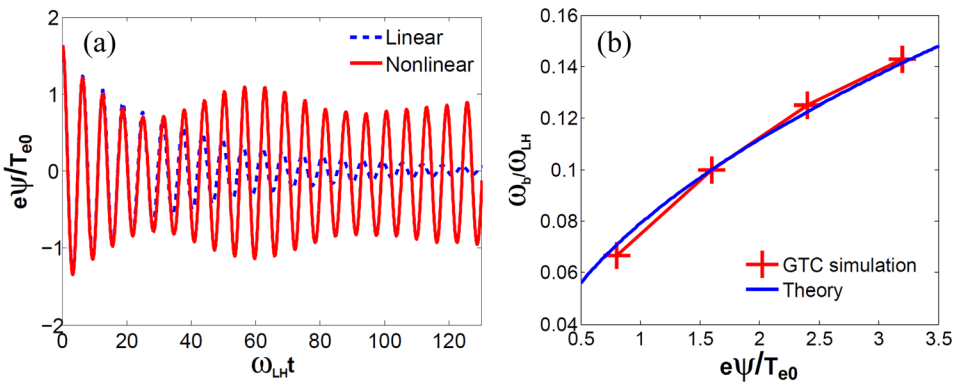


FIG. 4. (a)Nonlinear simulation of the LH wave exhibits oscillation in amplitude of the generalized potential (solid line), while linear simulation shows exponential decay (dashed line). (b) The comparison of the dependence of the bounce frequency on the wave amplitude between GTC nonlinear simulation and the theory.

solutions of the reduced model and the Maxwell model very well when $k_\perp/k_{||} \gg 1$. For typical experimental parameters, $k_\perp/k_{||} \gg 1$ can be satisfied for the LH waves in the core plasmas.[48,49]

Next, we use the initial perturbation method[46,47] to carry out the electromagnetic simulations of the linear and nonlinear Landau damping for the LH waves in hot plasmas, using an initial electron density perturbation with $k_{||} = 150.0\,\mathrm{m}^{-1}$. The plasma density $n_{e0} = n_{i0} = 7.6 \times 10^{13}\,\mathrm{cm}^{-3}$, electron temperature $T_{e0} = 6.0\,\mathrm{keV}$, and magnetic field $B = 2.0\,\mathrm{T}$ are uniform. In this parameter regime, both electrostatic and electromagnetic components are important to the LH wave dispersion relation, since it is the turning point of the mode conversion. The time histories of the generalized potential $\psi$ (as defined in Sec. II) of the LH waves with $\omega/(k_{||}v_{the}) \approx 3.2$ from the linear and nonlinear electromagnetic simulations are shown in Fig. 4(a). The red solid line shows that the amplitude oscillates in the nonlinear simulation, while the blue dashed line shows that the wave decays exponentially in the linear simulation. The oscillation of the LH wave amplitude in the nonlinear simulation is due to the wave trapping of the resonant electrons, and the oscillation (bounce) frequency agrees well with the theoretical prediction $\omega_b = k_{||}v_{the}\sqrt{e\psi/T_{e0}}$ as shown in Fig. 4(b). The particle trapping by waves is a basic phenomenon of the nonlinear wave–particle interaction.[52,53] The agreement between the simulation and the theory for the bounce frequency shows that our model captures the important nonlinear effects faithfully.

## VI. CONCLUSIONS

The nonlinear electromagnetic fluid (or fully kinetic) ion/DK electron model has been implemented into GTC for the LH wave study in the toroidal geometry. The DK electron model can be described by either the Hamiltonian formulation using canonical momentum or the symplectic formulation using kinetic momentum. The use of the electron continuity equation provides a better numerical performance, which avoids the numerical instability caused by the discrepancy between marker distribution with noise and the Maxwellian distribution in the $\delta f$ method simulation. Both the theoretical and numerical benchmarks of the dispersion relation of LH waves have been carried out, which show good agreements with the results from the Maxwell model when $k_\perp/k_{||} \gg 1$. In the nonlinear simulation of the LH wave damping in hot plasmas, we find that the amplitude of the wave field perturbation oscillates with a bounce frequency, which is due to the wave trapping of the resonant electrons. This frequency agrees well with the existing theoretical predictions. An importance sampling PIC scheme has been applied to simulate the LH wave propagation with high numerical resolution and efficiency. Compared to WKB and full-wave approaches based on the linear and quasi-linear theories, our PIC simulation model based on the first-principles can capture the nonlinear effects, which provides a powerful tool to study the nonlinear physics of LH waves in tokamak. Applications of this simulation model to the linear mode conversion, nonlinear current drive, and parametric decay instabilities of LH waves are reported in separate papers.[50,54]

## ACKNOWLEDGMENTS

This work was supported by China National Magnetic Confinement Fusion Science Program (Grant No. 2013GB111000) and U.S. Department of Energy (DOE) SciDAC GSEP Program. This work used resources of the Oak Ridge Leadership Computing Facility at Oak Ridge National Laboratory (DOE Contract No. DE-AC05-00OR22725) and the National Energy Research Scientific Computing Center (DOE Contract No. DE-AC02-05CH11231). J.B. acknowledges support from China Scholarship Council (Grant No. 201306010032), and encouragements from and useful discussions with L. Chen, N. J. Fisch, M. Porkolab, W. W. Lee, F. Zonca, J. C. Wright, Z. X. Lu, and GTC team.

## APPENDIX A: MOTION EQUATIONS OF THE DRIFT KINETIC ELECTRON IN MAGNETIC COORDINATES WITH FULLY ELECTROMAGNETIC PERTURBATIONS

The general magnetic flux coordinates system $(\psi, \theta, \zeta)$ has already been defined in Sec. IV. Then, the equilibrium magnetic field can be written either in contravariant form as Eq. (A1) or in covariant form as Eq. (A2)

$$\mathbf{B}_0 = q\nabla\psi \times \nabla\theta - \nabla\psi \times \nabla\zeta, \tag{A1}$$

$$\mathbf{B}_0 = \delta\nabla\psi + I\nabla\theta + g\nabla\zeta. \tag{A2}$$

The Jacobian in magnetic flux coordinates is

$$J^{-1} = \nabla\psi \cdot \nabla\theta \times \nabla\zeta = \frac{B_0^2}{gq + I}. \tag{A3}$$

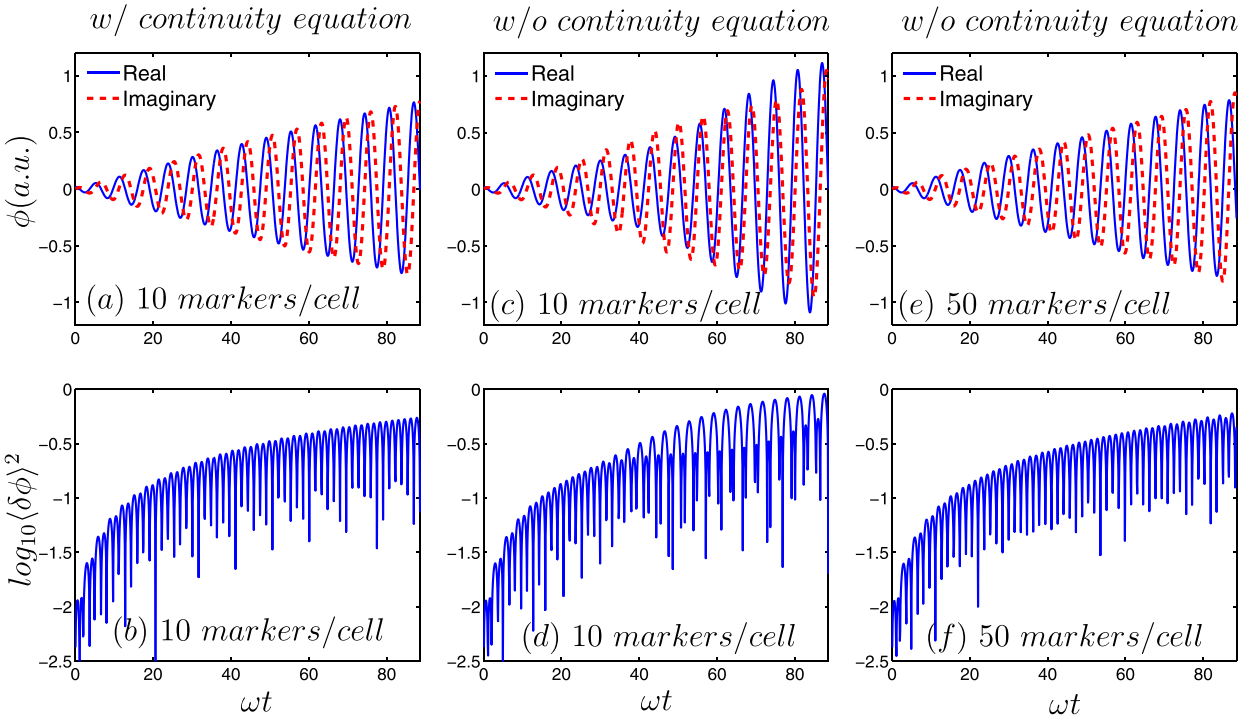


FIG. 5. Panels (a), (c), and (e) show the single mode histories of electrostatic potential, and panels (b), (d), and (f) show the amplitude histories. Panels (a) and (b) use 10 markers per cell and electron continuity equation. Panels (c) and (d) use 10 markers per cell but do not use electron continuity equation. Panels (e) and (f) use 50 markers per cell but do not use electron continuity equation.

Writing the particle motion equations of the drift kinetic Eqs. (4) and (10) into magnetic flux coordinates, we have

$$\dot{\psi} = \frac{c}{q_e}\frac{\partial \varepsilon_0}{\partial B_0}\left(\frac{I}{D}\frac{\partial B_0}{\partial \zeta} - \frac{g}{D}\frac{\partial B_0}{\partial \theta}\right) + c\left(\frac{I}{D}\frac{\partial \phi}{\partial \zeta} - \frac{g}{D}\frac{\partial \phi}{\partial \theta}\right) + v_{||}B_0\left(\frac{g}{D}\frac{\partial \alpha}{\partial \theta} - \frac{I}{D}\frac{\partial \alpha}{\partial \zeta}\right) + \frac{c\mu}{q_e}\left(\frac{I}{D}\frac{\partial \delta B_{||}}{\partial \zeta} - \frac{g}{D}\frac{\partial \delta B_{||}}{\partial \theta}\right), \tag{A4}$$

$$\dot{\theta} = \frac{v_{||}B_0(1-\rho_c g' - g\partial_\psi \alpha)}{D} + c\frac{g}{D}\left(\frac{1}{q_e}\frac{\partial \varepsilon_0}{\partial B_0}\frac{\partial B_0}{\partial \psi} + \frac{\partial \phi}{\partial \psi} + \frac{\mu}{q_e}\frac{\partial \delta B_{||}}{\partial \psi}\right), \tag{A5}$$

$$\dot{\zeta} = \frac{v_{||}B_0(q+\rho_c I' + I\partial_\psi \alpha)}{D} - c\frac{I}{D}\left(\frac{1}{q_e}\frac{\partial \varepsilon_0}{\partial B_0}\frac{\partial B_0}{\partial \psi} + \frac{\partial \phi}{\partial \psi} + \frac{\mu}{q_e}\frac{\partial \delta B_{||}}{\partial \psi}\right), \tag{A6}$$

$$\dot{\rho}_{||} = -c\frac{(1-\rho_c g' - g\partial_\psi \alpha)}{D}\left(\frac{1}{q_e}\frac{\partial \varepsilon}{\partial B_0}\frac{\partial B_0}{\partial \theta} + \frac{\partial \phi}{\partial \theta} + \frac{\mu}{q_e}\frac{\partial \delta B_{||}}{\partial \theta}\right) - c\frac{(q+\rho_c I' + I\partial_\psi \alpha)}{D}\left(\frac{1}{q_e}\frac{\partial \varepsilon}{\partial B_0}\frac{\partial B_0}{\partial \zeta} + \frac{\partial \phi}{\partial \zeta} + \frac{\mu}{q_e}\frac{\partial \delta B_{||}}{\partial \zeta}\right) + c\frac{(I\partial_\zeta \alpha - g\partial_\theta \alpha)}{D}\left(\frac{1}{q_e}\frac{\partial \varepsilon}{\partial B_0}\frac{\partial B_0}{\partial \psi} + \frac{\partial \phi}{\partial \psi} + \frac{\mu}{q_e}\frac{\partial \delta B_{||}}{\partial \psi}\right) - \frac{\partial \alpha}{\partial t}, \tag{A7}$$

$$\dot{\rho}_c = -c\frac{(1-\rho_c g')}{D}\left[\frac{1}{q_e}\frac{\partial \varepsilon}{\partial B_0}\frac{\partial B_0}{\partial \theta} + \frac{\partial \phi}{\partial \theta} + \frac{\mu}{q_e}\frac{\partial \delta B_{||}}{\partial \theta} - \frac{q_e}{m_e c^2}\rho_{||}B_0^2\frac{\partial \alpha}{\partial \theta}\right] - c\frac{(q+\rho_c I')}{D}\left(\frac{\partial \phi}{\partial \zeta} + \frac{\mu}{q_e}\frac{\partial \delta B_{||}}{\partial \zeta} - \frac{q_e}{m_e c^2}\rho_{||}B_0^2\frac{\partial \alpha}{\partial \zeta}\right), \tag{A8}$$

where $D = JB_0^2(1+\rho_c \mathbf{b}_0 \cdot \nabla \times \mathbf{b}_0) = gq + I + \rho_c(gI' - Ig')$, $I' = \partial I/\partial \psi$, $g' = \partial g/\partial \psi$, $\alpha = \delta A_{||}/B_0$, $\rho_{||} = v_{||}/\Omega_{ce}$, $\rho_c = \rho_{||} + \alpha$, and $\frac{\partial \varepsilon_0}{\partial B_0} = \mu + \frac{q_e^2}{m_{ec^2}}\rho_{||}^2 B_0$. Eqs. (A4)–(A8) describe the drift kinetic electron dynamics with fully electromagnetic perturbations in the magnetic flux coordinates, and they can reduce to the results from White and Chance[51] when $\delta B_{||} = 0$. Eqs. (A4)–(A6) and (A8) describe the particle motion of the drift kinetic electron with canonical momentum in Eq. (4), and Eqs. (A4)–(A7) describe the particle motion of the drift kinetic electron with kinetic momentum in Eq. (10).

## APPENDIX B: THE IMPORTANCE OF THE ELECTRON CONTINUITY EQUATION

Here, we carry out simulations of the antenna excitation of the LH wave with a single mode number to show the importance of the electron continuity equation on the numerical performance. In the simulation, the plasma equilibrium parameters are the same with the dispersion relation benchmark cases in Sec. V. The LH wave with frequency $\omega = 80.0\Omega_{ci}$ and parallel wave vector $k_{||} = 100.0\,\mathrm{m}^{-1}$ is chosen. In the first simulation, we use kinetic markers to calculate the electron perturbed velocity and use electron continuity equation to calculate the electron perturbed density. The mode and amplitude histories are shown in Figs. 5(a) and 5(b). It is found that the mode history has a good growth which is proportional to the time $t$. In the second simulation, we use the kinetic markers to calculate both the electron perturbed density and perturbed velocity in the simulation. We find that the real and imaginary parts of the LH wave do not match with each other, and the mode amplitude history has a large

numerical oscillation as shown in Figs. 5(c) and 5(d). Only after increasing the marker number can the real and imaginary parts match with each other as well as the first case as shown in Figs. 5(e) and 5(f).

By comparing these three cases, we find that applying electron continuity equation can help to suppress the numerical instability and reduce the computational cost as illustrated in Sec. II.


[1]N. J. Fisch, Phys. Rev. Lett. **41**, 873 (1978).
[2]N. J. Fisch, Rev. Mod. Phys. **59**, 175–234 (1987).
[3]C. Gormezano, A. C. C. Sips, T. C. Luce, S. Ide, A. Becoulet, X. Litaudon, A. Isayama, J. Hobirk, M. R. Wade, T. Oikawa, R. Prater, A. Zvonkov, B. Lloyd, T. Suzuki, E. Barbato, P. Bonoli, C. K. Phillips, V. Vdovin, E. Joffrin, T. Casper, J. Ferron, D. Mazon, D. Moreau, R. Bundy, C. Kessel, A. Fukuyama, N. Hayashi, F. Imbeaux, M. Murakami, A. R. Polevoi, and H. E. St. John, Nucl. Fusion **47**, S285–S336 (2007).
[4]A. H. Reiman, Phys. Fluids **26**, 1338 (1983).
[5]P. T. Bonoli and E. Ott, Phys. Fluids **25**, 359 (1982).
[6]J. C. Wright, P. T. Bonoli, A. E. Schmidt, C. K. Phillips, E. J. Valeo, R. W. Harvey, and M. A. Brambilla, Phys. Plasmas **16**, 072502 (2009).
[7]S. Shiraiwa, O. Meneghini, R. Parker, P. T. Bonoli, M. Garrett, M. C. Kaufman, J. C. Wright, and S. Wukitch, Phys. Plasma **17**, 056119 (2010).
[8]Z. X. Lu, F. Zonca, and A. Cardinali, Phys. Plasmas **20**, 032115 (2013).
[9]P. T. Bonoli and R. C. Englade, Phys. Fluids **29**, 2937 (1986).
[10]G. M. Wallace, R. R. Parker, P. T. Bonoli, A. E. Hubbard, J. W. Hughes, B. L. LaBombard, O. Meneghini, A. E. Schmidt, S. Shiraiwa, D. G. Whyte, J. C. Wright, S. J. Wukitch, R. W. Harvey, A. P. Smirnov, and J. R. Wilson, Phys. Plasmas **17**, 082508 (2010).
[11]M. Porkolab, S. Bernabei, W. M. Hooke, R. W. Motley, and T. Nagashima, Phys. Rev. Lett. **38**, 230 (1977).
[12]S. G. Baek, R. R. Parker, S. Shiraiwa, G. M. Wallace, P. T. Bonoli, D. Brunner, I. C. Faust, A. E. Hubbard, B. LaBombard, and M. Porkolab, Plasma Phys. Controlled Fusion **55**, 052001 (2013).
[13]S. G. Baek, S. Shiraiwa, R. R. Parker, P. T. Bonoli, E. S. Marmar, G. M. Wallace, A. Dominguez, G. J. Kramer, and C. Lau, Phys. Plasmas **21**, 012506 (2014).
[14]M. H. Li, B. J. Ding, J. Z. Zhang, K. F. Gan, H. Q. Wang, Y. Peysson, J. Decker, L. Zhang, W. Wei, Y. C. Li, Z. G. Wu, W. D. Ma, H. Jia, M. Chen, Y. Yang, J. Q. Feng, M. Wang, H. D. Xu, J. F. Shan, F. K. Liu, and EAST Team, Phys. Plasmas **21**, 062510 (2014).
[15]Y. Lin, X. Y. Wang, Z. Lin, and L. Chen, Plasma Phys. Controlled Fusion **47**, 657 (2005).
[16]L. Qi, X. Y. Wang, and Y. Lin, Phys. Plasmas **20**, 062107 (2013).
[17]D. H. Li, N. Xiang, Y. Lin, X. Y. Wang, C. Yang, and J. Ma, Plasma Sci. Technol. **16**, 821 (2014).
[18]C. Nieter and J. R. Cary, J. Comput. Phys. **196**, 448 (2004).
[19]C. Y. Gan, N. Xiang, J. Ou, and Z. Yu, Nucl. Fusion **55**, 063002 (2015).
[20]H. Qin and W. M. Tang, Phys. Plasmas **11**, 1052 (2004).
[21]Z. Yu and H. Qin, Phys. Plasmas **16**, 032507 (2009).
[22]A. Kuley, Z. X. Wang, Z. Lin, and F. Wessel, Phys. Plasmas **20**, 102515 (2013).
[23]J. Bao, Z. Lin, A. Kuley, and Z. X. Lu, Plasma Phys. Controlled Fusion **56**, 095020 (2014).
[24]Z. Lin, T. S. Hahm, W. W. Lee, W. M. Tang, and R. B. White, Science **281**, 1835 (1998).
[25]M. Porkolab, Phys. Fluids **17**, 1432 (1974).
[26]V. K. Tripathi, C. Grebogi, and C. S. Liu, Phys. Fluids **20**, 1525 (1977).
[27]C. S. Liu, V. K. Tripathi, V. S. Chan, and V. Stefan, Phys. Fluids **27**, 1709 (1984).
[28]R. Cesario, L. Amicucci, A. Cardinali, C. Castaldo, M. Marinucci, F. Napoli, F. Paoletti, D. De Arcangelis, M. Ferrari, A. Galli, G. Gallo, E. Pullara, G. Schettini, and A. A. Tuccillo, Nucl. Fusion **54**, 043002 (2014).
[29]X. Wei, Y. Xiao, A. Kuley, and Z. Lin, Phys. Plasmas **22**, 092502 (2015).
[30]A. Kuley, Z. Lin, J. Bao, X. Wei, Y. Xiao, W. L. Zhang, G. Y. Sun, and N. J. Fisch, Phys. Plasmas **22**, 102515 (2015).
[31]G. Hu and J. A. Krommes, Phys. Plasmas **1**, 863 (1994).
[32]W. W. Lee, T. G. Jenkins, and S. Ethier, Comput. Phys. Commun. **182**, 564–569 (2011).
[33]T. S. Hahm, W. W. Lee, and A. Brizard, Phys. Fluids **31**, 1940 (1988).
[34]A. J. Brizard and T. S. Hahm, Rev. Mod. Phys. **79**, 421 (2007).
[35]A. Brizard, Phys. Fluids B **4**, 1213 (1992).
[36]W. Deng, Z. Lin, and I. Holod, Nucl. Fusion **52**, 023005 (2012).
[37]Y. Lin, X. Y. Wang, L. Chen, X. Lu, and W. Kong, Plasma Phys. Controlled Fusion **53**, 054013 (2011).
[38]T. H. Stix, *Waves in Plasmas* (AIP, New York, 1992).
[39]I. Holod, W. L. Zhang, Y. Xiao, and Z. Lin, Phys. Plasmas **16**, 122307 (2009).
[40]Y. Xiao and Z. Lin, Phys. Rev. Lett. **103**, 085004 (2009).
[41]W. L. Zhang, Z. Lin, and L. Chen, Phys. Rev. Lett. **101**, 095001 (2008).
[42]H. S. Zhang, Z. Lin, and I. Holod, Phys. Rev. Lett. **109**, 025001 (2012).
[43]Z. Wang, Z. Lin, I. Holod, W. W. Heidbrink, B. Tobias, M. Van Zeeland, and M. E. Austin, Phys. Rev. Lett. **111**, 145003 (2013).
[44]J. McClenaghan, Z. Lin, I. Holod, W. Deng, and Z. X. Wang, Phys. Plasmas **21**, 122519 (2014).
[45]D. Liu, W. Zhang, J. McClenaghan, J. Wang, and Z. Lin, Phys. Plasmas **21**, 122520 (2014).
[46]W. Deng, Z. Lin, I. Holod, X. Wang, Y. Xiao, and W. Zhang, Phys. Plasmas **17**, 112504 (2010).
[47]H. Zhang, Z. Lin, I. Holod, X. Wang, Y. Xiao, and W. Zhang, Phys. Plasmas **17**, 112505 (2010).
[48]B. J. Ding, E. H. Kong, M. H. Li, L. Zhang, W. Wei, M. Wang, H. D. Xu, Y. C. Li, B. L. Ling, Q. Zang *et al.*, Nucl. Fusion **53**, 113027 (2013).
[49]J. R. Wilson, R. Parker, M. Bitter, P. T. Bonoli, C. Fiore, R. W. Harvey, K. Hill, A. E. Hubbard, J. W. Hughes, A. Ince-Cushman *et al.*, Nucl. Fusion **49**, 115015 (2009).
[50]J. Bao, Z. Lin, A. Kuley, and Z. X. Wang, Nucl. Fusion **56**, 066007 (2016).
[51]R. B. White and M. S. Chance, Phys. Fluids **27**, 2455 (1984).
[52]L. Chen, *Waves and Instabilities in Plasmas* (World Scientific, Singapore, 1987).
[53]Z. Lin and L. Chen, Phys. Plasmas **8**, 1447 (2001).
[54]J. Bao and Z. Lin, "Nonlinear absorption and parametric decay instability of lower hybrid waves in fusion plasmas" (unpublished).